Antibody-induced uncoating of human rhinovirus B14

Yangchao Dong[a,b,1], Yue Liu[a,1], Wen Jiang[a], Thomas J. Smith[c], Zhikai Xu[b], and Michael G. Rossmann[a,2]

[a]Department of Biological Sciences, Purdue University, West Lafayette, IN 47907; [b]Department of Microbiology, Faculty of Preclinical Medicine, Fourth Military Medical University, Xi'an 710032, China; and [c]Department of Biochemistry and Molecular Biology, University of Texas Medical Branch at Galveston, Galveston, TX 77555

Rhinoviruses (RVs) are the major causes of common colds in humans. They have a nonenveloped, icosahedral capsid surrounding a positive-strand RNA genome. Here we report that the antigen-binding (Fab) fragment of a neutralizing antibody (C5) can trigger genome release from RV-B14 to form emptied particles and neutralize virus infection. Using cryo-electron microscopy, structures of the C5 Fab in complex with the full and emptied particles have been determined at 2.3 Å and 3.0 Å resolution, respectively. Each of the 60 Fab molecules binds primarily to a region on viral protein 3 (VP3). Binding of the C5 Fabs to RV-B14 results in significant conformational changes around holes in the capsid through which the viral RNA might exit. These results are so far the highest resolution view of an antibody–virus complex and elucidate a mechanism whereby antibodies neutralize RVs and related viruses by inducing virus uncoating.

rhinovirus | antibody | cryo-electron microscopy | genome release | atomic structure

Rhinoviruses (RVs) belong to the *Enterovirus* (EV) genus of the *Picornaviridae*. The family consists of a diversity of nonenveloped, icosahedral viruses that possess a single strand of positive-sense RNA genome (1). Specifically, these viruses include a number of medically important human pathogens, such as RVs, foot-and-mouth disease virus, polioviruses, coxsackieviruses, echoviruses, EV-D68, EV-A71, and hepatitis A virus (2). Infection of RVs leads to both acute upper and lower respiratory tract diseases in humans, which cause a heavy burden for public health finance (3). There are three species of RVs based on sequence comparisons (RV-A, -B, and -C). Members of the species RV-A and RV-B have also been classified into two groups (major and minor) based on their receptor use for cell entry (4). The major group of RVs (e.g., RV-B14) use intercellular adhesion molecule 1 (ICAM-1), an Ig-like molecule, as a receptor, and the minor group RVs (e.g., RV-A2) use low-density lipoprotein receptor as a receptor. In contrast, members of the recently identified RV-C species use cadherin-related family member 3 as a cellular receptor (5).

The genomic RNA of RVs and other related picornaviruses encodes four capsid proteins, VP1–VP4. The capsid of these viruses has a size of ~300 Å in diameter and exhibits pseudo-T = 3 icosahedral symmetry (6). The icosahedral capsid shell is formed by 60 copies of VP1, VP2, and VP3, of which the N termini are located in the virus interior and the C termini decorate the virus external surface. These three polypeptides possess an eight-stranded antiparallel β-barrel "jelly roll" fold (7). In contrast, VP4 has an extended structure, and 60 copies of VP4 reside inside the capsid. In addition, the capsid shows a star-shaped mesa on each fivefold vertex that is surrounded by a ~25 Å deep canyon. The canyon region of major receptor group RVs is responsible for binding ICAM-1 (8).

Binding of ICAM-1 to RV-B14, as also binding of other Ig-like receptors to their respective EVs, at physiological temperatures results in dramatic structural rearrangements of the capsid that triggers virus uncoating (9, 10). Upon attachment onto host cells via receptor binding, the native infectious virions (150S) are converted into A(altered)-particles (135S), which are characterized by

the loss of VP4 and externalization of the VP1 N-terminal residues (11). The A-particles were proposed to release the genomic RNA within host cells and to become emptied B-particles (80S) (12, 13). Thus, the A-particles were considered to be an intermediate state in the uncoating pathway (14). Therefore, conformational changes of the capsid are crucial to viral entry and are triggered by interaction with the host cell.

Host humoral immune response, based on antibodies, represents a major defense line against virus infections. Antibodies can neutralize virus infections by binding to specific regions, namely epitopes, on the virus outer surface. Nonenveloped viruses, including picornaviruses, can be neutralized by antibodies that prevent virus attachment onto host cells and/or stabilize the virus to impede virus uncoating (15). A recent study reported that a neutralizing antibody E18 caused genome release of EV-A71, thereby discovering a new mechanism of neutralization (16). Nevertheless, the current understanding of antibody-induced uncoating is largely limited by a lack of high-resolution structures of picornavirus–antibody complexes. Furthermore, it remains unknown whether antibody-induced virus uncoating is a mechanism shared by many picornaviruses.

In the present work, cryo-electron microscopy (cryo-EM) analyses were performed using RV-B14 and a murine neutralizing monoclonal antibody (mAb) C5, which had previously been proposed to bind the neutralizing immunogenic (NIm)-III site on the RV-B14 outer surface (6). The NIm-III site is located primarily on VP3 and represents one of the four major NIm sites on RVs, as determined by studies of neutralizing antibody escape mutants using a panel of mAbs against RV-B14 (17, 18).

> ## Significance
>
> Rhinoviruses (RVs) frequently cause respiratory infections in humans. However, there are currently no approved antiviral treatments or vaccines available. Using cryo-electron microscopy (cryo-EM), we have shown that the antigen-binding fragment of a neutralizing antibody, C5, binds to RV-B14 and causes significant structural rearrangements of the capsid to allow release of the viral genome. C5-induced virus uncoating depends upon temperature and virus–Fab molar ratio. These results present so far the highest resolution cryo-EM structures of a virus–antibody complex and suggest a conserved mechanism whereby antibodies neutralize infections by RVs and related viruses via induction of premature genome release from the capsid.

BIOPHYSICS AND COMPUTATIONAL BIOLOGY

Here we show that binding of the antigen-binding (Fab) fragments of C5 to RV-B14 causes native full virions to release the genomic RNA in a temperature- and virus–Fab molecular ratio-dependent manner. During Fab-induced uncoating, the capsid undergoes particle expansion to form pores at twofold axes through which the viral RNA might exit. Our results suggest that C5 Fab might preferentially select the expanded conformation of the capsid over the unexpanded conformation to facilitate virus uncoating.

Results and Discussion

Cryo-EM Reconstructions of RV-B14 Complexed with C5 Fab. The Fab fragment of C5 was incubated with RV-B14 under three different conditions by varying the incubation temperature and virus–Fab molar ratio. This resulted in three cryo-EM datasets (set-a, set-b, and set-c) (Table S1). When the Fab and the virus were incubated with a ratio of ~180 Fab per virion at 33 °C for 1 h (dataset set-a), EM micrographs showed the presence of a mixed population of full and empty particles. There were 30–60% of empty particles as estimated by visual inspection of the micrographs (Fig. S1). Furthermore, 2D classification of individual particle images extracted from the micrographs separated full (set-a-full) and empty (set-a-empty) particles and showed prominent spikes on the outer surface of both types of particles (Fig. S1). This indicated that both types of particles were bound by Fab molecules. In contrast, when the temperature was changed to 4 °C (set-b) or the molar ratio was changed to ~60 Fab per virion (set-c), empty particles that showed spike-like densities on the particle outer surface only accounted for less than 0.5% of all particles.

The observation that full and empty particles coexist under the same incubation condition (set-a) provides a basis for comparison. If the molar ratio (Fabs per binding site) is decreased from 3:1 (set-a) to 1:1 (set-b), the Fab molecules are unable to cause the virus to lose its genome. Similarly, if the temperature is decreased while keeping the molar ratio the same (set-a to set-c), then also the Fab fails to cause release of the genome. These results demonstrate that C5 Fab can induce genome release of RV-B14 in a temperature- and virus–Fab molar ratio-dependent manner.

After 2D classification, a dataset of 46,684 full particles (set-a-full) and a dataset of 9,521 empty particles (set-a-empty) were selected from set-a; also, 23,090 full particles (set-b-full) were selected from set-b, and 36,866 particles (set-c-full) were selected from set-c. A "gold standard" single particle icosahedral reconstruction strategy was independently applied to each of these four sets of particle images using the program jspr (19, 20). High-resolution refinements involved parameters that define particle orientation, particle center, phase error due to beam tilt, astigmatism, defocus, magnification, and anisotropic magnification distortion. The resolutions of the final reconstructions are 2.5 Å for set-a-full, 3.0 Å for set-a-empty, 2.7 Å for set-b-full, and 2.3 Å for set-c-full (Fig. 1 and Figs. S1–S3), respectively, as determined by the Fourier shell correlation (FSC) between two half maps using the criterion of FSC = 0.143 (21).

Conformational Changes Associated with Viral Genome Release. The capsid structures of all three full particle–Fab complexes are essentially the same, as is evident from the root-mean-square deviation (rmsd = 0.2–0.7 Å) between equivalent Cα atoms for each pair of structures when icosahedral symmetry axes are aligned (Table S2). In contrast, the capsid structure of the empty particle–Fab complex is significantly different from any of the full-particle structures (rmsd = 5.5–6.1 Å) (Table S2). The VP1 N-terminal residues 1001–1060, VP2 residues 2043–2056, VP3 residues 3172–3181, and the VP4 residues are disordered in empty particles. (Residues are numbered by adding 1,000 to VP1 residues, 2,000 to VP2 residues, 3,000 to VP3 residues, and 4,000 to VP4 residues.) These observations suggest that the VP1 N-terminal residues might be externalized and that VP4 might be lost from the empty particle, because these residues reside in the interior of the full
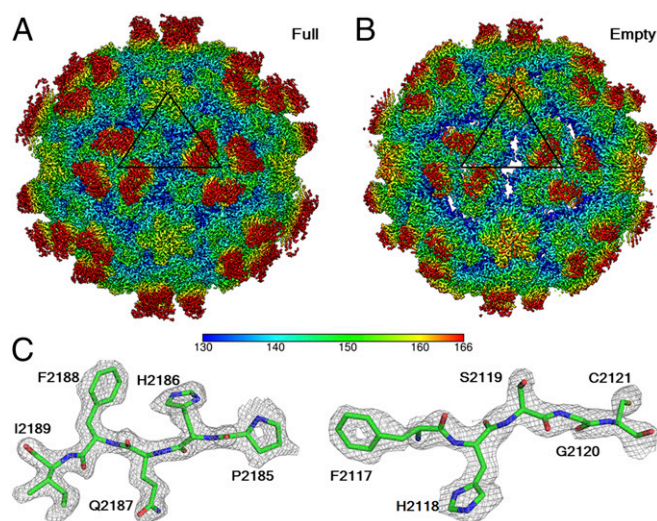
particle. It has been suggested that externalization of these internal residues facilitates interactions of the capsid with host cell membranes during cell entry of EVs (22, 23).

The empty particle structure (set-a-empty) is expanded by about 12 Å in diameter with respect to the full-particle structure (set-a-full). This expansion is caused primarily by movements of VP1, VP2, and VP3 as individual rigid bodies, because the jelly roll β-barrel of each capsid protein in the full-particle structure can be superimposed with its counterpart in the empty particle structure with rmsds of 1.0 Å (VP1), 0.5 Å (VP2), and 0.9 Å (VP3) (Fig. S4). Specifically, VP1, VP2, and VP3 are moved away from the virus center by 6.6 Å, 3.9 Å, and 5.1 Å and rotated by 2.5°, 5.7°, and 4.3°, respectively (Table 1). As a consequence, an α-helix in VP2 (residues 2091–2098) and its twofold-related helix move away from each other. These structural changes lead to the formation of roughly rectangular (25 Å × 8 Å) pores around the icosahedral twofold axes through which the viral RNA and VP4 might exit (Figs. 1 and 2) (24, 25). In addition, because of the rigid body movements and the disordering of residues 3172–3181 in the VP3 GH loop (the loop that links β-strands G and H), pores are opened up near the quasi-threefold axes (Fig. 1), which probably allow for the externalization of VP1 N-terminal residues as previously suggested (26, 27).

The buried surface areas at the interface between any pair of capsid proteins within one protomer (VP1, VP2, and VP3 as defined in ref. 6) of the empty particle are similar to those in the full particle (Table S3). Thus, the respective protomers in these two forms of particles were superimposed for structural comparison. Within the protomer, VP2, VP3, and the fivefold distant regions of VP1 in the two structures are well aligned to each other, with an rmsd of 1.4 Å. Nevertheless, the jelly roll β-barrel and fivefold proximal loops of VP1 undergo a hinge-like motion with a translation of 1.1 Å and a rotation of 7.5°, which helps maintain interactions between amino acid residues near the fivefold axes. Furthermore, the VP2 C-terminal tail (residues 2253–2260) near each twofold axis is located on the outer surface of the full particle. In the empty particle, the tail is displaced by an rmsd of 17.7 Å between equivalent Cα atoms (Fig. S5). These residues are internalized and interact with VP3 in the neighboring, fivefold-related protomer and with VP2 in the neighboring, twofold-related protomer (Fig. 2). As a result, the

Fig. 1. Cryo-EM reconstructions of RV-B14 in complex with the C5 Fab. The maps of C5 Fab complexed with full (*A*) and empty (*B*) particles are colored based on the radial distance (Å) of the capsid and Fab from the particle center. Only the front half of each type of particle is shown. Triangles indicate an icosahedral asymmetric unit. (*C*) Typical cryo-EM map densities at 2.3 Å resolution.

Dong et al.

Table 1. Translation and rotation of individual capsid proteins during virus uncoating

Protein	Rmsd,[a] Å	Translation, Å	Rotation,[b] °	Psi,[c] °	Phi,[c] °
VP1	1.0	6.6	2.5	74.8	30.8
VP2	0.5	3.9	5.7	61.6	12.0
VP3	0.9	5.1	4.3	76.4	12.0

[a]Based on equivalent Cα atoms in the jelly roll β-barrel between the full and empty particles.
[b]Counterclockwise rotation.
[c]The direction of the rotational axis is defined by these two polar angles according to ref. 63.

tail participates in forming the aforementioned pores at twofold axes and probably contributes to stabilize the particle. Such structural change of the VP2 C-terminal tail has not been previously observed in other A-particle or empty particle-like structures of EVs (13, 27).

In all three full-particle maps, but not in the empty-particle map, there is a region together with its icosahedral twofold-related counterpart that forms density around each twofold axis at the capsid inner surface. The density height of this region is about 4 σ above the mean of the cryo-EM map (set-c-full, unsharpened map, and low passed to 3 Å resolution), whereas densities for the main chain of surrounding amino acids are about 13 σ high. This region, which probably represents ordered viral RNA, can accommodate about six ribonucleotide residues. In addition, it is in close proximity to the VP1 N-terminal residues 1022–1027 and the VP2 N-terminal residues 2037–2039 (Fig. 2). These observations reinforce the suggestion that the viral RNA probably exits through the pore at a twofold axis upon externalization of internal residues including the VP1 N-terminal residues.

Interactions between RV-B14 and C5 Fab. The 2.3 Å resolution cryo-EM map of set-c-full shows well-ordered densities of residue side chains at the binding interface between C5 Fab and the capsid (Fig. S6). Despite a lack of experimentally determined sequence information on C5, a close-to-authentic amino acid sequence of the variable region was generated by taking advantage of high-resolution map density features and 499 homologous X-ray crystal structures of murine antibodies (*Materials and Methods*).

In all four structures of RV-B14 complexed with C5 Fab, nearly the same set of capsid protein residues is identified to interact with the variable heavy (VH) domain and variable light (VL) domain of C5. Each of the 60 Fab molecules binds to only one protomer by contacting a threefold proximal region on the virus outer surface (Fig. 3A). This region, in which the NIm-III

site is covered, is formed mainly by residues in the VP1 C terminus, VP2 C terminus, VP3 N terminus, VP3 BC loop, and VP3 HI loop (Fig. S7). The footprint of C5 Fab on RV-B14 is similar to that of E18 Fab on EV-A71 (16). Both Fabs act as an inducer of virus uncoating in vitro and neutralize virus infection in cell-based plaque reduction neutralization tests (Fig. 3B). These observations suggest that NIm-III–binding neutralizing antibodies might use a common neutralizing mechanism by triggering genome release of EVs. In contrast, previous structural studies on antibodies that target other NIm sites on RV-B14 or homologous sites on other EVs have not shown that these antibodies cause virus uncoating (28–32).

Mechanism of C5 Fab-Induced Virus Uncoating. C5 Fab has a footprint on RV-B14 that does not have any overlap with that of ICAM-1 (Fig. S8). Nor do any of the 60 Fab molecules clash with ICAM-1 when an ICAM-1 molecule (Ig-like domains 1–2) is docked onto the C5 Fab-bound full particle (Fig. S8). Nevertheless, the temperature dependency of C5 Fab-triggered genome release is reminiscent of ICAM-1–induced uncoating of RV-B14 and related RVs in vitro (10, 33). In both cases, virus uncoating does not or rarely occurs at 4 °C, whereas the capsid becomes expanded upon receptor or Fab binding at physiological temperatures. This is due in large part to the observation that physiological temperatures favor virus breathing. In this process, the virus reversibly externalizes internal amino acid residues and undergoes particle expansion/shrinkage (34). Furthermore, as in the crystal structure of RV-B14 (6), the full-particle structures presented here do not contain a "pocket factor" in the hydrophobic pocket of the VP1 jelly roll. Because the pocket factor, a fatty acid-like molecule, contributes to stabilizing many other EVs (35–37), the absence of this stabilizing factor in RV-B14 would facilitate virus breathing at physiological temperatures. Thus, it is probable that binding of C5 Fab to the virus, much like receptor binding to the virus, shifts the equilibrium to the expanded conformation, which might have a higher affinity to C5 Fabs than the nonexpanded conformation (38). In this way, C5 Fab can lead to irreversible structural changes of the virus and induce virus uncoating, as does receptor binding (38).

Unlike ICAM-1, binding of C5 Fab to the virus at physiological temperatures does not lead to the formation of an A-particle or A-particle–like intermediate state, which exhibits an expanded capsid that contains the viral RNA (11, 27). This observation indicates that a higher activation energy barrier probably exists in the process of C5-Fab–induced virus uncoating than that required for ICAM-1–induced virus uncoating. Compatible with this prediction, a threshold of virus–C5 Fab molar ratio between 1:60 and
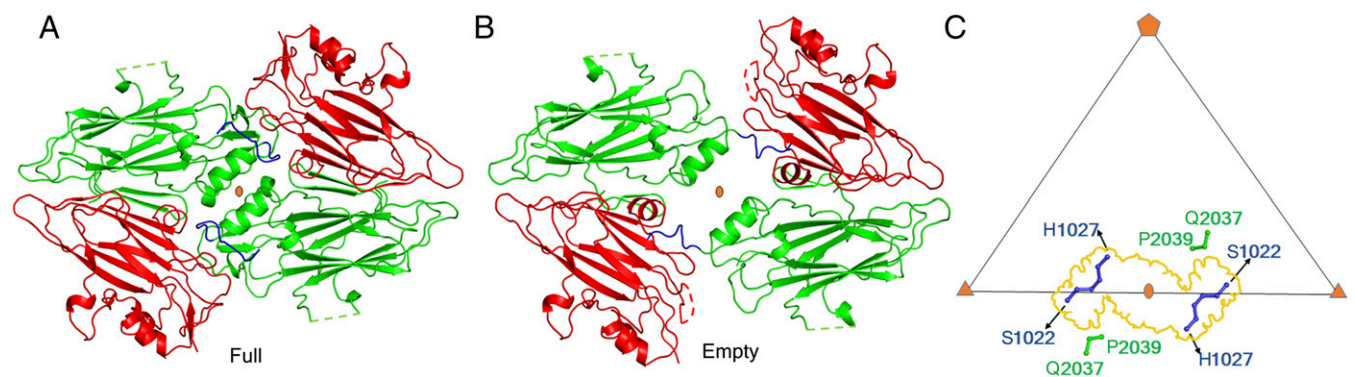

Fig. 2. Pores around the icosahedral twofold axes in the empty particle. Comparison of the twofold proximal regions of the full (A) and empty (B) particles. The ribbon diagrams are colored: VP2 C-terminal residues 2253–2260 (blue) and the remaining residues of VP2 (green) and VP3 (red). (C) Density at the capsid's inner surface in the full particles around the twofold axes probably represents ordered RNA. A yellow contour outlines the density when looking out from the inside of the particle along a twofold axis. Surrounding residues are colored blue (VP1) and green (VP2).
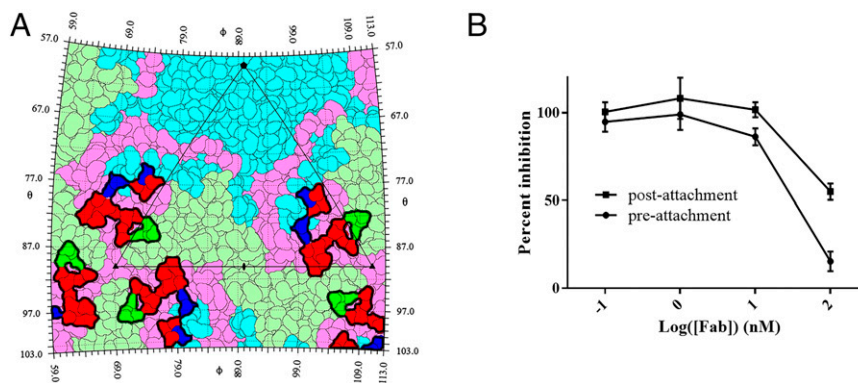
Dong et al.

BIOPHYSICS AND COMPUTATIONAL BIOLOGY

Fig. 3. The C5 Fab binds to a threefold proximal region on RV-B14. (*A*) A map of the RV-B14 surface residues is colored by viral polypeptides: VP1 (light blue), VP2 (light green), and VP3 (light red). Residues that interact with C5 Fab are highlighted in blue (VP1), green (VP2), and red (VP3), respectively. These residues are within a distance of 4 Å from any atom of the bound C5 Fab. The black contour outlines the footprint of C5 Fab. (*B*) The C5 Fab exhibits neutralizing activity against RV-B14 infection. The virus concentration used in the experiments was about 3×10^{-8} nM, assuming a particle-to-plaque forming unit ratio of about 200 (62). Shown is a plot of percent inhibition as a function of the logarithm of the Fab concentration. Error bars indicate SDs.

1:180 is necessary to cross the energy barrier and to cause virus uncoating (Table S1). In contrast, a single Ig-like receptor molecule can induce local structural rearrangements of an EV near the receptor binding site that primes the virus for uncoating (39). An analogous process would be anticipated when ICAM-1 interacts with RV-B14. Nevertheless, it is currently not clear what accounts for these differences between C5 Fab and ICAM-1–triggered virus uncoating, which awaits future investigations.

Similar to the observations on RV-B14 presented here, an early study reported that the full virions of poliovirus were converted into emptied particles upon antibody binding (40). Nevertheless, antibody-induced uncoating of poliovirus only occurred under conditions that had a much lower ionic strength than physiological conditions. Likewise, a low ionic strength medium was previously shown to facilitate heat-induced EV uncoating in vitro (11–13, 41). In contrast, C5 Fab causes RV-B14 uncoating at physiological ionic strength, as does E18 Fab to EV-A71 (16). Thus, it is probable that both antibodies might be capable of triggering premature viral genome release in vivo. Moreover, the report also indicated that antibody molecules did not remain bound to the emptied particles of poliovirus after neutralization, because the emptied particles did not exhibit suitable epitopes that would allow antibody binding (40). Nevertheless, C5 Fabs bind to the emptied particles of RV-B14. Moreover, comparison of the emptied particle structure with the full-particle structure shows that the Cα atom positions of residues that form the footprint of C5 Fab do not have significant changes (Figs. S4, S5, and S7). Thus, the footprint of the aforementioned antibody on poliovirus is probably different from that of C5 on RV-B14.

In summary, the present work has extended the discovery of antibody-caused viral genome release to another member of the EV, RV-B14. Thus, antibody-induced uncoating might be a conserved mechanism for many EVs. The high-resolution cryo-EM structures presented here provide the molecular basis for the design of immunogens to elicit antibodies that neutralize EV infections via induction of premature virus uncoating.

Materials and Methods

Virus Growth and Purification. RV-B14 was grown in HeLa-H1 (ATCC CRL195) cells and purified as described previously (42, 43). Briefly, cells were infected by RV-B14 (multiplicity of infection = 2) for 24–36 h until complete cytopathic effect was observed. The supernatant and infected cells were separated by centrifugation. The cell pellets were subjected to four freeze–thaw cycles followed by Dounce homogenization. Upon centrifugation and removal of cell debris, the virus-containing supernatant was combined with the aforementioned supernatant and spun down at $277{,}937 \times g$ for 2 h using a Beckman Ti 50.2 rotor. The resultant pellets were resuspended in buffer

A (250 mM NaCl, 250 mM Hepes, pH 7.5) and then treated sequentially with DNase (0.01 mg/mL), RNase (7.5 mg/mL), and trypsin (0.8 mg/mL). Subsequently, 15 mM EDTA and 1% (wt/vol) sodium n-lauroyl sarcosinate were added. After centrifugation at $277{,}937 \times g$ for 2 h, the pellets were resuspended in buffer A and sedimented through a 10–40% potassium tartrate gradient at $221{,}830 \times g$ for 90 min using a Beckman SW41 Ti rotor. Purified viruses, as also C5 Fab, were kept in buffer B (120 mM NaCl, 20 mM Tris·HCl, 1 mM EDTA, pH 8.0).

Antibody Production and Fab Generation. Hybridoma cells were grown in CELLine CL 1000 bioreactors using RPMI 1640 media. Every 3 d, 10–15 mL of cell suspension was removed from the cellular growth chamber. Cells were removed via a 15-min centrifugation at $10{,}000 \times g$. Antibody was purified from the supernatant using protein G affinity chromatography as previously described (44). In brief, mAbs were purified from cell culture supernatant with a 5-mL HiTrap Protein G HP column (GE Healthcare). The column was first equilibrated with 20 mM sodium phosphate buffer (pH 7.0), and the supernatant was passed over the column and washed with several volumes of 20 mM sodium phosphate buffer (pH 7.0). The bound antibody was eluted with 50 mM sodium citrate buffer (pH 2.0), and the pH was quickly raised to neutrality using 1 M Tris buffer, pH 7.6. Purified antibody was prepared for digestion by dialysis against 0.1 M sodium phosphate buffer, pH 7.0. β-mercaptoethanol was added to a final concentration of 25 mM, and papain was added at a ratio of 1:500 (papain:antibody). Digestion was allowed to proceed for 2 h, and the reaction was quenched by the addition of 50 mM (final concentration) iodoacetamide. After papain digestion, the sample was dialyzed against 50 mM Tris (pH 7.6) and then purified using a Mono-Q column (GE Healthcare) equilibrated with the same Tris buffer and then eluted with a sodium chloride gradient using 1 M NaCl in the same buffer.

Cryo-EM Sample Preparation and Data Acquisition. Purified RV-B14 was incubated with the Fab fragment of mAb C5 under three different conditions: 180 Fab molecules per virion at 33 °C for 1 h (set-a), 180 Fab molecules per virion at 4 °C for 1 h (set-b), and 60 Fab molecules per virion at 33 °C for 1 h (set-c) (Table 1). The final concentration of RV-B14 was about 0.7 mg/mL. Lacey carbon grids (Ted Pella Inc.) were glow-discharged for 2 min. Then 3-μL poly-L-lysin solution [0.1% (wt/vol) in H₂O; Sigma] was applied onto the grid surface and incubated for ~2 min at room temperature. Upon blotting, 2.5 μL of the virus–Fab complex was applied onto the grid, which was blotted for about 7 s, and subsequently plunge-frozen into liquid ethane using a cryo-plunge 3 system (Gatan). The humidity of the chamber was kept at about 85%.

A Titan Krios cryo-electron microscope (FEI, 300 kV) equipped with a K2 Summit direct electron detector (Gatan) was used for data acquisition at liquid nitrogen temperature. For set-a and set-b, cryo-EM images of frozen, hydrated virus–Fab complexes were automatically recorded at a nominal magnification of 29,000× in electron counting mode using the program Leginon (45), giving a physical pixel size of 1.00 Å per pixel at the specimen level. The defocus range was 0.3–6.6 μm for set-a and 1.3–6.0 μm for set-b. The dose rate was ~5 e⁻/pixel/s. A total dose of about 30 e⁻/Å² was fractionated into 50 frames with a frame rate of 120 ms. For set-c, cryo-EM images were recorded at a nominal magnification of 22,500× in superresolution mode with

www.manaraa.com

a physical pixel size of 1.30 Å per pixel at the specimen level and with a defocus range of 0.7–5.8 μm. The dose rate was ∼8 e−/pixel/s. A total dose of ∼33 e−/Å² was fractionated into 38 frames with a frame rate of 200 ms. Statistics for data collection were summarized in Table S1.

Image Processing. The following procedures were performed using programs as integrated in the image processing pipeline Appion (46). To correct the stage drift and beam-induced motion during exposure, individual frames of each movie were aligned using the program MotionCorr (47). All of the aligned frames were summed up to produce individual micrographs. The micrographs that had severe drift and ice contamination were discarded based upon inspection of the power spectra. Contrast transfer function (CTF) parameters were then estimated using the program CTFFIND3 (48). Particles were automatically picked up on each micrograph using templates that were generated based on a small set of manually selected particles. A combination of the programs FindEM (49) and DoG picker (50) was used in this process. Upon particle boxing and extraction, a total of 60,065, 26,759, and 39,728 particles were obtained for set-a, set-b, and set-c, respectively.

For each of the three sets, the particle images were eight times (set-c) or four times (set-a and set-b) binned and subsequently subjected to reference-free 2D classification using the program Relion (51), which sorted out junk particles and separated empty particles from full particles. This produced four datasets: set-a-full (46,684 full particles from set-a), set-a-empty (9,521 empty particles from set-a), set-b-full (23,090 full particles from set-b), and set-c-full (36,866 full particles from set-c). A gold-standard 3D reconstruction strategy was applied to each of these four datasets using the program jspr as previously described (19, 52). Icosahedral symmetry was imposed in this process. Every dataset was divided into two halves. The following procedures were the same for the two halves. An initial model was generated from experimental images. The parameters for particle orientation and center of each experimental particle image were refined against the initial model. A new 3D model was reconstructed from particle images using the newly determined particle orientation and center. Iterative refinement cycles improved the accuracy of particle orientation and center determination. The refinement procedures were extended to four times binned, two times binned, and unbinned data. Finally, parameters for particle orientation, particle center, astigmatism, defocus, magnification, phase error due to beam shift, and anisotropic magnification distortion (53) were included in refinement. To achieve 3D reconstructions with the highest possible resolution, particle images were re-extracted from micrographs that were generated by summing up the aligned frames 4–49 (set-a and set-b) or frames 3–16 (set-c). The final map was obtained by averaging the two independent half maps in real space and sharpened with a negative B factor and with an FSC curve-based low-pass filter using the program Relion (21, 51). The map resolution was estimated based on the FSC (0.143 as a cutoff) between the two half maps (unsharpened) (21). The statistics are summarized in Table S1.

Atomic Model Building and Refinement. The crystal structure of RV-B14 [Protein Data Bank (PDB) ID code 4RHV] was manually fitted into the final cryo-EM map using the program Chimera (54). The resultant atomic model was subjected to multiple cycles of model rebuilding using the program Coot (55) and real space refinement against the map using the program Phenix (56). This procedure yielded an atomic model of the capsid that fit well into the cryo-EM density as judged by visual inspection.

Given that the amino acid sequence of the C5 antibody was not available, a close-to-authentic amino acid sequence for the variable region (VH domain and VL domain) of C5 was obtained based on the high-resolution features of cryo-EM map density (set-c-full) and homologous X-ray crystal structures. These

structures (a total of 499), with a resolution of no worse than 3.0 Å, were of murine antibodies available in the database SabDab (57) as of January 2017. A section of the cryo-EM map (set-c-full) was generated by selecting grid points within a radius of 6 Å around every atom of the VH and VL domains of a homologous structure (PDB ID code 1BBJ) that had been fitted into the map density. 1BBJ was not included in the 499 structures. For each of the 499 homologous structures, all regions other than domains VH and VL were excluded. The resultant atomic model was fitted into and subsequently refined in real space against the aforementioned section of the map. The top eight structures that gave the highest correlation coefficient (CC) between the section of the map and a density map calculated from the coordinates were selected for amino acid sequence alignments. At this point, an atomic model of the VH and VL domains of C5 Fab was built using the structure (PDB ID code 1A7R) with the highest CC as a template. At a given position, if the top eight antibodies do not share the same amino acid, the amino acid at such position in 1A7R was changed to an alanine or an aromatic residue that occurred in one of the eight sequences and that fit well into the cryo-EM map density as judged by visual inspection. If the top eight antibodies all have the same amino acid at a position, the amino acid residue was retained.

Next, the coordinates of the capsid and the variable region of C5 Fab were combined. A section of the cryo-EM map was generated by selecting grid points within a radius of 5 Å around each atom of the resultant atomic model. This section of the map was used to calculate pseudo-crystallographic structure factors (space group P1), against which the atomic model was refined in reciprocal space using the program Phenix (56). Specifically, atomic positions, individual B factors, and occupancies were refined. The new atomic model was subsequently refined against the original cryo-EM map in real space with 60-fold noncrystallographic symmetry constraints using Phenix. Water molecules were added using Coot (55). Model validation was based on the criteria of MolProbity (58). Figures were produced using the programs Chimera (54) and Pymol (https://www.pymol.org/). Structural comparisons were performed using the program HOMOLOGY (59). Buried surface areas were calculated using the program PISA (60). Roadmaps were produced using the program RIVEM (61).

Plaque Reduction Neutralization Test. The Fab fragment was diluted in Dulbecco's Modified Eagle's medium (DMEM) to reach a series of concentrations (0.1–100 nM). For the preattachment neutralizing assay, Fab solution with a given dilution or DMEM only (control) was incubated with RV-B14 (100 pfu per well) for 1 h at 33 °C. The mixture (1 mL) was inoculated onto HeLa-H1 cell monolayers (∼85% confluency) for an additional 1 h at 33 °C. For the postattachment neutralization assay, RV-B14 was allowed to attach onto HeLa-H1 cells for 1 h at 33 °C followed by addition of Fab solution or DMEM only (control) and by an additional 1-h incubation at 33 °C. Next, the following procedures were applied to both preattachment and postattachment neutralization assays. In essence, media was aspirated before 2 mL of overlay [0.8% (wt/vol) agarose and 2% (vol/vol) FBS in DMEM] was added. Plates were incubated at 33 °C with 5% CO_2 for 4 d and stained with phenol red. Percent inhibition was calculated as $(N_{control} - N_{fab})/N_{control} \times 100\%$, where $N_{control}$ is the mean of plaque counts for control wells and N_{fab} represents the plaque count observed in a well in which a given concentration of Fab was added. All experiments were performed in triplicate.

1. Racaniello VR (2007) Picornaviridae: The viruses and their replication. *Fields Virology*, eds Knipe DM, Howley PM (Lippincott Williams & Wilkins, Philadelphia), 5th Ed, Vol 1, pp 796–839.
2. Knowles NJ, et al. (2012) Picornaviridae. *Virus Taxonomy: Classification and Nomenclature of Viruses: Ninth Report of the International Committee on Taxonomy of Viruses*, eds King AMQ, Adams MJ, Carstens EB, Lefkowitz EJ (Elsevier, San Diego, CA), pp 855–880.
3. Turner RB, Couch RB (2007) Rhinoviruses. *Fields Virology*, eds Knipe DM, Howley PM (Lippincott Williams & Wilkins, Philadelphia), 5th Ed, Vol 1, pp 895–911.
4. Palmenberg AC, Gern JE (2015) Classification and evolution of human rhinoviruses. *Methods Mol Biol* 1221:1–10.
5. Bochkov YA, et al. (2015) Cadherin-related family member 3, a childhood asthma susceptibility gene product, mediates rhinovirus C binding and replication. *Proc Natl Acad Sci USA* 112:5485–5490.
6. Rossmann MG, et al. (1985) Structure of a human common cold virus and functional relationship to other picornaviruses. *Nature* 317:145–153.
7. Rossmann MG, Johnson JE (1989) Icosahedral RNA virus structure. *Annu Rev Biochem* 58:533–573.
8. Olson NH, et al. (1993) Structure of a human rhinovirus complexed with its receptor molecule. *Proc Natl Acad Sci USA* 90:507–511.
9. Kaplan G, Freistadt MS, Racaniello VR (1990) Neutralization of poliovirus by cell receptors expressed in insect cells. *J Virol* 64:4697–4702.
10. Hoover-Litty H, Greve JM (1993) Formation of rhinovirus-soluble ICAM-1 complexes and conformational changes in the virion. *J Virol* 67:390–397.
11. Bubeck D, et al. (2005) The structure of the poliovirus 135S cell entry intermediate at 10-angstrom resolution reveals the location of an externalized polypeptide that binds to membranes. *J Virol* 79:7745–7755.
12. Hewat EA, Blaas D (2004) Cryoelectron microscopy analysis of the structural changes associated with human rhinovirus type 14 uncoating. *J Virol* 78:2935–2942.
13. Garriga D, et al. (2012) Insights into minor group rhinovirus uncoating: The X-ray structure of the HRV2 empty capsid. *PLoS Pathog* 8:e1002473.

Dong et al.

BIOPHYSICS AND COMPUTATIONAL BIOLOGY

www.manaraa.com

14. Huang Y, Hogle JM, Chow M (2000) Is the 135S poliovirus particle an intermediate during cell entry? *J Virol* 74:8757–8761.

15. Smith TJ (2011) Structural studies on antibody recognition and neutralization of viruses. *Curr Opin Virol* 1:150–156.

16. Plevka P, et al. (2014) Neutralizing antibodies can initiate genome release from human enterovirus 71. *Proc Natl Acad Sci USA* 111:2134–2139.

17. Sherry B, Rueckert R (1985) Evidence for at least two dominant neutralization antigens on human rhinovirus 14. *J Virol* 53:137–143.

18. Sherry B, Mosser AG, Colonno RJ, Rueckert RR (1986) Use of monoclonal antibodies to identify four neutralization immunogens on a common cold picornavirus, human rhinovirus 14. *J Virol* 57:246–257.

19. Guo F, Jiang W (2014) Single particle cryo-electron microscopy and 3-D reconstruction of viruses. *Methods Mol Biol* 1117:401–443.

20. Scheres SHW, Chen S (2012) Prevention of overfitting in cryo-EM structure determination. *Nat Methods* 9:853–854.

21. Rosenthal PB, Henderson R (2003) Optimal determination of particle orientation, absolute hand, and contrast loss in single-particle electron cryomicroscopy. *J Mol Biol* 333:721–745.

22. Fricks CE, Hogle JM (1990) Cell-induced conformational change in poliovirus: Externalization of the amino terminus of VP1 is responsible for liposome binding. *J Virol* 64:1934–1945.

23. Panjwani A, et al. (2014) Capsid protein VP4 of human rhinovirus induces membrane permeability by the formation of a size-selective multimeric pore. *PLoS Pathog* 10: e1004294.

24. Harutyunyan S, et al. (2013) Viral uncoating is directional: Exit of the genomic RNA in a common cold virus starts with the poly-(A) tail at the 3′-end. *PLoS Pathog* 9: e1003270.

25. Katpally U, Fu T-M, Freed DC, Casimiro DR, Smith TJ (2009) Antibodies to the buried N terminus of rhinovirus VP4 exhibit cross-serotypic neutralization. *J Virol* 83: 7040–7048.

26. Lin J, et al. (2011) An externalized polypeptide partitions between two distinct sites on genome-released poliovirus particles. *J Virol* 85:9974–9983.

27. Ren J, et al. (2013) Picornavirus uncoating intermediate captured in atomic detail. *Nat Commun* 4:1929.

28. Smith TJ, et al. (1993) Structure of human rhinovirus complexed with Fab fragments from a neutralizing antibody. *J Virol* 67:1148–1158.

29. Liu H, et al. (1994) Structure determination of an Fab fragment that neutralizes human rhinovirus 14 and analysis of the Fab-virus complex. *J Mol Biol* 240:127–137.

30. Wien MW, et al. (1995) Structure of the complex between the Fab fragment of a neutralizing antibody for type 1 poliovirus and its viral epitope. *Nat Struct Biol* 2: 232–243.

31. Che Z, et al. (1998) Antibody-mediated neutralization of human rhinovirus 14 explored by means of cryoelectron microscopy and X-ray crystallography of virus-Fab complexes. *J Virol* 72:4610–4622.

32. Lin J, Cheng N, Hogle JM, Steven AC, Belnap DM (2013) Conformational shift of a major poliovirus antigen confirmed by immuno-cryogenic electron microscopy. *J Immunol* 191:884–891.

33. Xing L, Casasnovas JM, Cheng RH (2003) Structural analysis of human rhinovirus complexed with ICAM-1 reveals the dynamics of receptor-mediated virus uncoating. *J Virol* 77:6101–6107.

34. Lin J, et al. (2012) Structure of the Fab-labeled "breathing" state of native poliovirus. *J Virol* 86:5959–5962.

35. Filman DJ, et al. (1989) Structural factors that control conformational transitions and serotype specificity in type 3 poliovirus. *EMBO J* 8:1567–1579.

36. Smyth M, Pettitt T, Symonds A, Martin J (2003) Identification of the pocket factors in a picornavirus. *Arch Virol* 148:1225–1233.

37. Smith TJ, et al. (1986) The site of attachment in human rhinovirus 14 for antiviral agents that inhibit uncoating. *Science* 233:1286–1293.

38. Carson SD (2014) Kinetic models for receptor-catalyzed conversion of coxsackievirus B3 to A-particles. *J Virol* 88:11568–11575.

39. Lee H, et al. (2016) The novel asymmetric entry intermediate of a picornavirus captured with nanodiscs. *Sci Adv* 2:e1501929.

40. Brioen P, Rombaut B, Boeyé A (1985) Hit-and-run neutralization of poliovirus. *J Gen Virol* 66:2495–2499.

41. Wetz K, Kucinski T (1991) Influence of different ionic and pH environments on structural alterations of poliovirus and their possible relation to virus uncoating. *J Gen Virol* 72:2541–2544.

42. Zhao R, et al. (1996) Human rhinovirus 3 at 3.0 A resolution. *Structure* 4:1205–1220.

43. Liu Y, et al. (2015) Structure and inhibition of EV-D68, a virus that causes respiratory illness in children. *Science* 347:71–74.

44. Kolawole AO, et al. (2014) Flexibility in surface-exposed loops in a virus capsid mediates escape from antibody neutralization. *J Virol* 88:4543–4557.

45. Suloway C, et al. (2005) Automated molecular microscopy: The new Leginon system. *J Struct Biol* 151:41–60.

46. Lander GC, et al. (2009) Appion: An integrated, database-driven pipeline to facilitate EM image processing. *J Struct Biol* 166:95–102.

47. Li X, et al. (2013) Electron counting and beam-induced motion correction enable near-atomic-resolution single-particle cryo-EM. *Nat Methods* 10:584–590.

48. Mindell JA, Grigorieff N (2003) Accurate determination of local defocus and specimen tilt in electron microscopy. *J Struct Biol* 142:334–347.

49. Roseman AM (2004) FindEM–A fast, efficient program for automatic selection of particles from electron micrographs. *J Struct Biol* 145:91–99.

50. Voss NR, Yoshioka CK, Radermacher M, Potter CS, Carragher B (2009) DoG Picker and TiltPicker: Software tools to facilitate particle selection in single particle electron microscopy. *J Struct Biol* 166:205–213.

51. Scheres SHW (2012) RELION: Implementation of a Bayesian approach to cryo-EM structure determination. *J Struct Biol* 180:519–530.

52. Liu Y, et al. (2016) Atomic structure of a rhinovirus C, a virus species linked to severe childhood asthma. *Proc Natl Acad Sci USA* 113:8997–9002.

53. Yu G, et al. (2016) An algorithm for estimation and correction of anisotropic magnification distortion of cryo-EM images without need of pre-calibration. *J Struct Biol* 195:207–215.

54. Pettersen EF, et al. (2004) UCSF Chimera–A visualization system for exploratory research and analysis. *J Comput Chem* 25:1605–1612.

55. Emsley P, Lohkamp B, Scott WG, Cowtan K (2010) Features and development of Coot. *Acta Crystallogr D Biol Crystallogr* 66:486–501.

56. Adams PD, et al. (2010) PHENIX: A comprehensive Python-based system for macromolecular structure solution. *Acta Crystallogr D Biol Crystallogr* 66:213–221.

57. Dunbar J, et al. (2014) SAbDab: The structural antibody database. *Nucleic Acids Res* 42:D1140–D1146.

58. Chen VB, et al. (2010) MolProbity: All-atom structure validation for macromolecular crystallography. *Acta Crystallogr D Biol Crystallogr* 66:12–21.

59. Rossmann MG, Argos P (1975) A comparison of the heme binding pocket in globins and cytochrome b5. *J Biol Chem* 250:7525–7532.

60. Krissinel E, Henrick K (2007) Inference of macromolecular assemblies from crystalline state. *J Mol Biol* 372:774–797.

61. Xiao C, Rossmann MG (2007) Interpretation of electron density with stereographic roadmap projections. *J Struct Biol* 158:182–187.

62. Lee WM, Wang W (2003) Human rhinovirus type 16: Mutant V1210A requires capsid-binding drug for assembly of pentamers to form virions during morphogenesis. *J Virol* 77:6235–6244.

63. Rossmann MG, Blow DM (1962) The detection of sub-units within the crystallographic asymmetric unit. *Acta Crystallogr* 15:24–31.

Dong et al.